ACS AuthorChoice

JACS
JOURNAL OF THE AMERICAN CHEMICAL SOCIETY

Communication

pubs.acs.org/JACS

Terms of Use

Nanoscale Electrocatalysis: Visualizing Oxygen Reduction at Pristine, Kinked, and Oxidized Sites on Individual Carbon Nanotubes

Joshua C. Byers, Aleix G. Güell, and Patrick R. Unwin*

Department of Chemistry, University of Warwick, Gibbet Hill Road, Coventry, CV4 7AL, U.K.

Supporting Information

ABSTRACT: There is a prevailing and widely adopted view that carbon nanotubes, which are finding considerable application in energy, healthcare, and electronics applications, are highly (electro)catalytically inert unless modified, doped, or defected. By visualizing the electrochemical reduction of oxygen (hydrogen peroxide generation) at high resolution along pristine (defect-free) regions of individual single-walled carbon nanotubes, we show that there is, in fact, significant activity comparable to that of standard gold electrocatalysts. Moreover, the activity is greatly enhanced at strained (kinked) sites and regions modified by oxidation. Single-walled carbon nanotubes are thus effective electrocatalysts in their own right and not just supports for other materials.

Carbon nanotubes (CNTs) are being actively explored for a wide range of applications due to their exceptional electronic and surface properties.[1−3] The high surface area to mass ratio makes CNTs particularly promising candidates for applications in catalysis and energy conversion, but CNTs have, hitherto, largely been used as support materials for catalytic nanoparticles or molecules.[4−7] Indeed, there is a popular perception that pristine CNTs function only as support materials to wire up more active electrocatalytic materials, unless modified or doped.[8,9] Here, we demonstrate that high quality pristine single-walled carbon nanotubes (SWNTs) actually exhibit exceptional electrocatalytic properties for hydrogen peroxide (H_2O_2) generation via the oxygen reduction reaction (ORR). This is an important reaction because electrocatalysis is emerging as a potential route for H_2O_2 synthesis (300 million tons/annum industrial), and new electrocatalysts are actively being explored.[10] On the other hand, H_2O_2 is an unwanted byproduct of the ORR in polymer electrolyte membrane fuel cells, where CNTs are being widely considered as supports,[11] reducing the efficiency and being detrimental to cathode stability. These disparate applications highlight the need to better understand the ORR and H_2O_2 generation at SWNTs.

The ORR can occur via a direct 4-electron process (pathway 1) or an indirect pathway, which involves two sequential 2-electron-transfer steps (pathways 2 and 3) where peroxide is produced as an intermediate.[12]

$$O_2 + 2H_2O + 4e^- \rightleftharpoons 4OH^- \qquad E^\circ = +0.401\ \text{V vs NHE} \qquad (1)$$

$$O_2 + 2H_2O + 2e^- \rightleftharpoons H_2O_2 + 2OH^- \qquad E^\circ = -0.133\ \text{V vs NHE} \qquad (2)$$

$$H_2O_2 + 2e^- \rightleftharpoons 2OH^- \qquad E^\circ = +0.935\ \text{V vs NHE} \qquad (3)$$

For most carbon electrode materials, the ORR occurs via the indirect peroxide pathway.[13,14] It is well established that there is a very large overpotential on graphite, whereas kinetic measurements on SWNTs have proved difficult because of issues in defining electrode areas, materials properties, and mass transport in conventional electrode setups.[3]

Herein, we study the ORR at well-defined individual SWNTs using our recently developed multi-probe platform based on scanning electrochemical cell microscopy (SECCM),[15] that permits high-resolution reaction mapping of substrates to be correlated with local structure (Supporting Information (SI), sections 1−3).[16−20] The technique provides a means of positioning a tiny meniscus electrochemical cell on a substrate of interest that serves as a working electrode, whose area is defined by the meniscus diameter (Figure 1a).[19,20] By coupling this approach with complementary techniques (SEM, Raman) applied to the same area, detailed structure−activity correlations are revealed (SI, sections 1 and 3).[20] This approach is particularly powerful as it allows us to investigate structure−activity relationships of individual nanoscale features. Thus, we quantitatively capture and characterize the ORR at segments of straight and kinked pristine SWNTs and investigate the impact of deliberately oxidizing SWNTs.

A more detailed description of the SECCM operation can be found in the SI and elsewhere.[16,17] Briefly, a silanized theta pipet, that was pulled to a sub-micrometer diameter, was filled with an aerated phosphate buffer solution (pH 7.2, Sigma-Aldrich) and 25 mM KCl. Nanoscale electrochemical imaging was realized by translating the resulting meniscus confined electrochemical cell, formed at the theta pipet, over the substrate in the *xyz* directions with nanometer control. The substrate functioned as a working electrode whose potential was controlled using Ag/AgCl quasi-reference counter electrodes (QRCEs). An electrochemical current was measured when the meniscus made contact with the SWNT (Figure 1). Millimeter long flow aligned SWNTs were grown on an insulating Si/SiO_2 substrate using catalyzed chemical vapor deposition (SI, section 1), which allowed us to probe the

Received: June 6, 2014
Published: July 25, 2014

   dx.doi.org/10.1021/ja505708y | J. Am. Chem. Soc. 2014, 136, 11252−11255

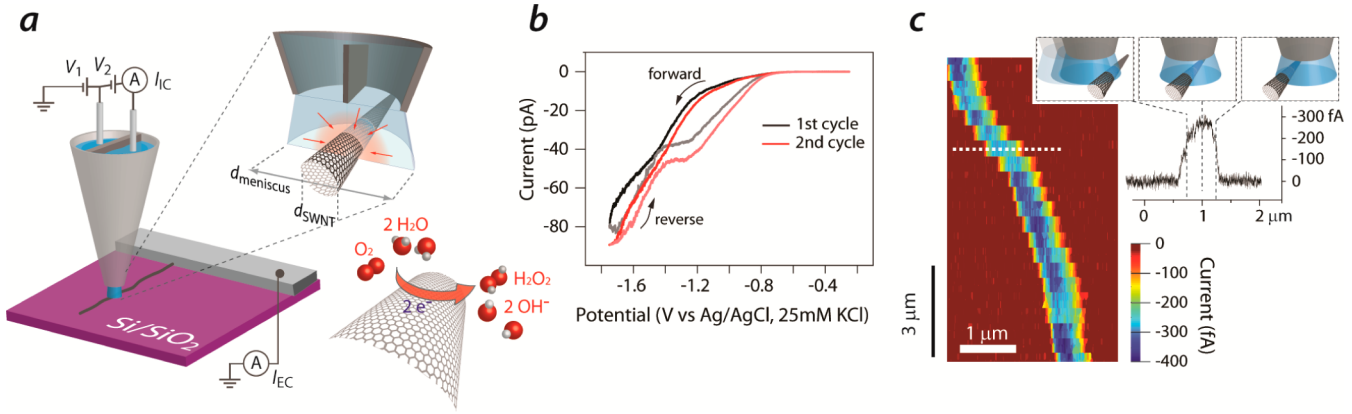

Figure 1. (a) SECCM setup showing a theta pipet positioned directly above an individual SWNT creating a well-defined tiny meniscus electrochemical cell for local electrochemical measurements and substrate mapping. A voltage, V_1, permits control of the working electrode potential, while an ion current (I_{IC}) between the two barrels of the pipet, generated by V_2, is used for precise pipet positioning. An electrochemical current (I_{EC}) is measured when the meniscus makes contact with the SWNT. Illustration (not to scale) of the enhanced mass transport and well-defined geometry of the SECCM setup, where $d_{meniscus}$ and d_{SWNT} correspond to meniscus and SWNT diameter, respectively. (b) Cyclic voltammograms of the ORR at a pristine *individual* SWNT. Scan rate: 100 mV/s. (c) Electrochemical map recorded at a substrate potential of −1.0 V vs Ag/AgCl QRCE for a pristine *individual* SWNT. Inset contains a line scan profile illustrating the evolution of the measured electrochemical current as the meniscus advanced across the SWNT. All measurements carried out in aerated PBS (pH 7.2) with 25 mM KCl.

electrochemical activity of individual SWNTs. Pd metal was evaporated onto the SWNTs at one end using a shadow mask to form an ohmic contact for electrical connection. The working electrode dimensions were determined by the diameter of the SWNT, d_{SWNT}, and the diameter of the meniscus, $d_{meniscus}$, as shown in Figure 1a.

Figure 1b shows a cyclic voltammogram (CV) of the ORR at a fixed position on an individual metallic SWNT. The metallic nature and diameter of the SWNT were determined by Raman spectroscopy (SI, Figure S2). Two separate waves were observed for both the forward (cathodic-going) and reverse (anodic-going) scans of the CV, but these were more pronounced in the anodic scan direction. The corresponding current plateaus ca. −1.25 and −1.70 V vs Ag/AgCl QRCE during the reverse scan indicate a 2-electron reduction to H_2O_2 (pathway 2) followed by further reduction to water (pathway 3) at SWNTs, as found in studies of CNT ensembles.[14] Measurements under similar conditions for highly oriented pyrolytic graphite (SI, Figure S3) revealed a much more negative onset potential (by >0.5 V), highlighting that for these two sp^2 carbon materials, the ORR is greatly facilitated on SWNTs compared to graphite. The hysteresis between the forward and reverse current−voltage response for SWNTs was most pronounced for the first wave, for the reduction of oxygen to H_2O_2 (pathway 2). This effect was fairly reversible, with similar behavior seen in the cathodic and anodic scan directions during the second voltammetric cycle, with a small increase in the limiting current. Chemical oxidation of the SWNT sidewall by the electrochemical generation of H_2O_2 is unlikely to occur to a significant extent due to its rapid flux away from the electrode as a result of the high mass transport of SECCM with a SWNT.[20] Permanent surface modification of the SWNT surface during the ORR also cannot account for the reversible nature of the hysteresis, and more likely reflects changes in the electrochemical double layer and interfacial structure over the wide potential range investigated.[14,21]

The electrochemical map in Figure 1c shows the oxygen reduction activity over a 10 µm length of a pristine metallic SWNT just at the onset potential (−1.0 V vs Ag/AgCl QRCE) where any differences in activity along the SWNT would be expected to be revealed. In fact, the electrochemical response is quite uniform over this long section and represents the intrinsic activity of an unmodified SWNT. Since the average defect spacing on SWNTs of this type is ∼4 µm,[22] which is much larger than the spatial resolution in the image (∼0.5 µm, Figure 1c) and in the line profiles (data acquired every 0.5 nm in the scan direction, Figure 1c), it can be readily deduced that there is little influence of defects in this electrochemical regime. In particular, the line profile morphology, in which the current increases monotonically, reaching a maximum, and then falls as the SECCM meniscus passes over the SWNT, is consistent with uniform SWNT electroactivity at the high spatial resolution (∼nm) of this measurement.[20,23,24]

Electrochemical[8] and chemical oxidation[25] has recently been used to increase the number of defect sites along the sidewalls of multiwalled CNTs to enhance their electrocatalytic activity toward the ORR. Increased defect densities at kinked regions of pristine SWNTs have also been confirmed through selective electrochemical deposition,[22] and our technique allowed us to probe the ORR directly in such regions. Figure 2a shows a large-scale electrochemical map of a section of a pristine SWNT that contained a kinked region, and Figure 2b shows a separately recorded zoom map of the kinked region. Considerably enhanced electrochemical activity is observed, as confirmed by the line profiles over this area (Figure 2b), highlighting the significant extent to which the activity is enhanced, revealed here using SECCM, as a result of the increased number of defects at these regions. Complementary maps obtained simultaneously during all SECCM measurements[20] were used to confirm that the meniscus footprint and effective volume were very consistent over the whole image and so the enhanced activity in the kink region can be assigned to the SWNT architecture and not to changes in the meniscus size. See SI, section S5, for further discussion and an example of the complementary maps obtained.

Enhancement of the ORR by defect sites was further confirmed by their intentional introduction along the SWNT sidewall by electrochemical oxidation (inset Figure 3a), which is known to introduce defects and oxygen functionalized moieties into the sp^2-hybridized carbon lattice.[26] Using SECCM, it was

dx.doi.org/10.1021/ja505708y | J. Am. Chem. Soc. 2014, 136, 11252−11255

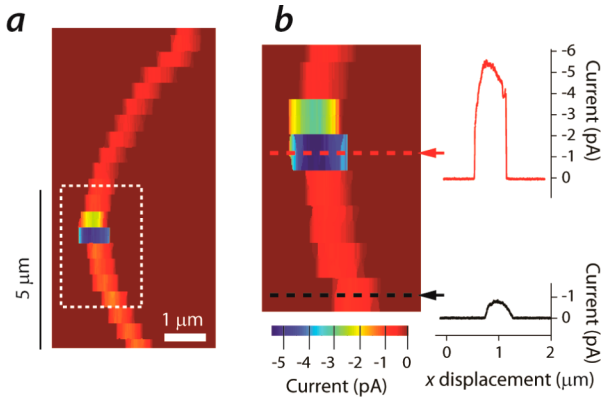

Figure 2. (a) Electrochemical map of a pristine SWNT that contained a kinked region. (b) Separate zoom-in electrochemical map of (a). Line scans of kinked region (red dashed line in (b)) and pristine site (black dashed line in (b)) highlighted in map (b). Maps obtained at −1.0 V vs Ag/AgCl QRCE.

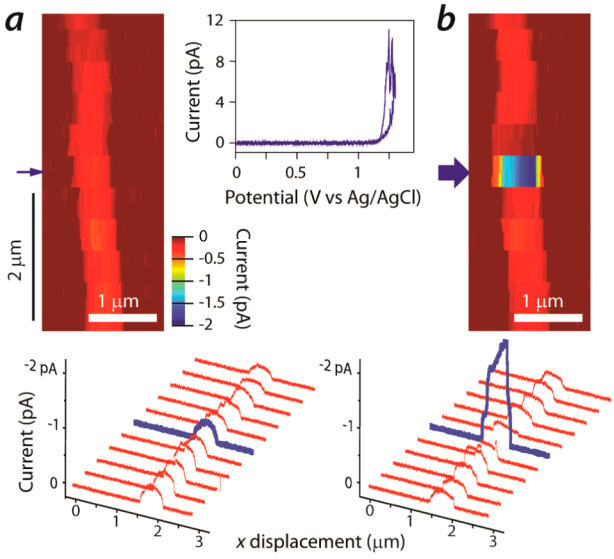

Figure 3. Electrochemical maps and line scans of a pristine SWNT before (a) and after (b) electrochemical oxidation; start and end potential 0 V, return potential 1.30 V at a scan rate of 50 mV/s (inset of (a)). Maps obtained at −0.75 V vs Ag/AgCl QRCE.

possible to directly compare variations in the electrochemical response in the same area of the SWNT before and after electrochemical oxidation of the SWNT sidewall (Figure 3a,b). Prior to electrochemical oxidation, a straight section of SWNT showed essentially uniform electrochemical activity along its length (Figure 3a). Activity measurements were made at a low driving potential of −0.75 V vs Ag/AgCl QRCE, to highlight any changes in electrochemical activity due to local electrochemical oxidation. With the SECCM meniscus fixed over the SWNT, the electrode potential was then scanned from 0 to 1.30 V and back to 0 V at a scan rate of 50 mV/s, resulting in an anodic current above ∼1.1 V. Following electrochemical oxidation, the ORR in the modified and surrounding region was re-imaged, revealing a 5-fold increase in electrochemical current in the modified region, and an asymmetric profile with discrete features, consistent with a heterogeneously active surface. It is further evident that following activation, the electrochemical response along the sidewall remained uniform on either side of the modified region confirming that there was no disconnection or cutting of the SWNT in this one terminal device.

It was possible to construct mass transport corrected Tafel plots to determine the exchange current density, j_0 (at zero overpotential), by extrapolation. The area of the cylindrical SWNT working electrode was defined by the meniscus diameter, d_{meniscus}, representing the length of the cylinder, while the effective width of exposed SWNT, W_{SWNT}, was given by $(\pi/2)d_{\text{SWNT}}$.[24] The meniscus width was determined accurately from a line scan of the SWNT, and was comparable with the diameter of the pipet itself, measured from an FE-SEM micrograph of the complementary theta pipet to that used for imaging (SI, Figure S5). The kinetic current density was then determined by correcting for mass transport using the following expression:

$$\frac{1}{j} = \frac{1}{j_k} + \frac{1}{j_d} \tag{4}$$

where j is the current density, j_k is the kinetic current density, and j_d is the diffusion-limited current density. Further details of the Tafel analysis, in which currents were further normalized by oxygen concentration, to permit comparison with published studies, are provided in the SI, section S6.

Tafel analysis of ORR (H_2O_2 generation) voltammograms (Figure 4) allowed comparison of the performance of pristine

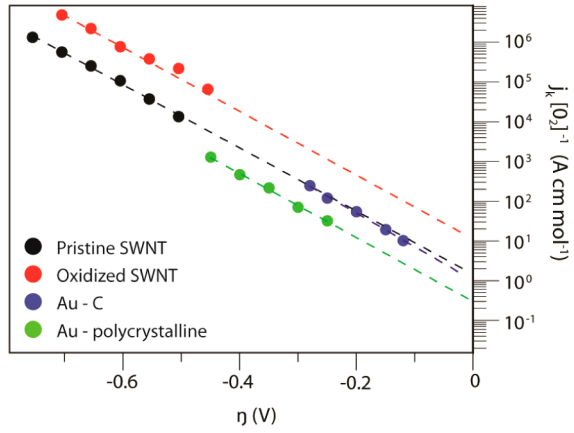

Figure 4. Mass transport corrected Tafel plots. The kinetic current density ordinates have been normalized by the oxygen concentration for each system to permit direct comparison. Kinetic current density, electrode potential, and experimental conditions for Au−C and Au−polycrystalline were obtained from refs 10, 27, and 28.

(black dots) and modified (red dots) SWNT portions to Au-polycrystalline (green dots) and Au−C (blue dots) electrodes, as well-known standards for electrochemical H_2O_2 electrogeneration.[27,28] Note that the overpotential is much higher for the SWNT system as a consequence of the ultrahigh mass transport rates generated in the SWNT-SECCM format,[20] leading to very high current density values. It is evident that the activity (current density) of the sidewall of pristine SWNTs is very similar to Au-based electrodes. Moreover, the oxidation of a SWNT provides an electrocatalyst for oxygen reduction where the reaction kinetics is approximately 1 order of magnitude larger than for Au-based electrodes. Thus, pristine SWNTs stand out as effective electrocatalysts and this activity can be further enhanced by electrochemical modification.

There is increasing interest in developing catalysts for the ORR that selectively promote H_2O_2 generation and permit

dx.doi.org/10.1021/ja505708y | J. Am. Chem. Soc. 2014, 136, 11252−11255

decentralized production.[29] From this perspective, SWNTs represent a powerful nonmetal electrocatalyst, where the activity can be tailored (enhanced) by building in particular architectures (kinks) or through surface modification (sidewall oxidation). On the other hand, the relative ease of H_2O_2 production at SWNTs may limit their use as supports for the development of stable fuel cell electrodes and in some healthcare applications where reactive oxygen species need to be avoided. In general, pristine SWNTs are not inert: they exhibit substantial intrinsic electrochemical activity, which needs to be taken into account in directing their use in the future.

■ ASSOCIATED CONTENT

Supporting Information

SWNT synthesis, experimental setup, Raman spectroscopy, and additional details of the Tafel analysis. This material is available free of charge via the Internet at http://pubs.acs.org.

■ AUTHOR INFORMATION

Corresponding Author

p.r.unwin@warwick.ac.uk

Notes

The authors declare no competing financial interest.

■ ACKNOWLEDGMENTS

We thank the European Research Council (ERC-2009-AdG247143-QUANTIF) for support. The research leading to these results has received funding from the European Union Seventh Framework Programme (FP7/2007-2013) under grant agreement no. 329953.

■ REFERENCES

(1) Balasubramanian, K.; Kern, K. *Adv. Mater.* **2014**, *26*, 1154.
(2) Wang, G. P.; Zhang, L.; Zhang, J. J. *Chem. Soc. Rev.* **2012**, *41*, 797.
(3) Dumitrescu, I.; Unwin, P. R.; Macpherson, J. V. *Chem. Commun.* **2009**, 6886.
(4) Le Goff, A.; Artero, V.; Jousselme, B.; Tran, P. D.; Guillet, N.; Metaye, R.; Fihri, A.; Palacin, S.; Fontecave, M. *Science* **2009**, *326*, 1384.
(5) Krishnan, S.; Armstrong, F. A. *Chem. Sci.* **2012**, *3*, 1015.
(6) Andreiadis, E. S.; Jacques, P. A.; Tran, P. D.; Leyris, A.; Chavarot-Kerlidou, M.; Jousselme, B.; Matheron, M.; Pecaut, J.; Palacin, S.; Fontecave, M.; Artero, V. *Nat. Chem.* **2013**, *5*, 48.
(7) Kongkanand, A.; Kuwabata, S.; Girishkumar, G.; Kamat, P. *Langmuir* **2006**, *22*, 2392.
(8) Gong, K.; Du, F.; Xia, Z.; Durstock, M.; Dai, L. *Science* **2009**, *323*, 760.
(9) Li, Y.; Zhou, W.; Wang, H.; Xie, L.; Liang, Y.; Wei, F.; Idrobo, J. C.; Pennycook, S. J.; Dai, H. *Nat. Nanotechnol.* **2012**, *7*, 394.
(10) Siahrostami, S.; Verdaguer-Casadevall, A.; Karamad, M.; Deiana, D.; Malacrida, P.; Wickman, B.; Escudero-Escribano, M.; Paoli, E. A.; Frydendal, R.; Hansen, T. W.; Chorkendorff, I.; Stephens, I. E. L.; Rossmeisl, J. *Nat. Mater.* **2013**, *12*, 1137.
(11) Wildgoose, G. G.; Banks, C. E.; Compton, R. G. *Small* **2006**, *2*, 182.
(12) Kleijn, S. E. F.; Lai, S. C. S.; Koper, M. T. M.; Unwin, P. R. *Angew. Chem., Int. Ed.* **2014**, *53*, 3558.
(13) Yeager, E. *Electrochim. Acta* **1984**, *29*, 1527.
(14) Kruusenberg, I.; Alexeyeva, N.; Tammeveski, K. *Carbon* **2009**, *47*, 651.
(15) Ebejer, N.; Schnippering, M.; Colburn, A. W.; Edwards, M. A.; Unwin, P. R. *Anal. Chem.* **2010**, *82*, 9141.
(16) Snowden, M. E.; Güell, A. G.; Lai, S. C. S.; McKelvey, K.; Ebejer, N.; O'Connell, M. A.; Colburn, A. W.; Unwin, P. R. *Anal. Chem.* **2012**, *84*, 2483.
(17) Ebejer, N.; Güell, A. G.; Lai, S. C. S.; McKelvey, K.; Snowden, M. E.; Unwin, P. R. *Annu. Rev. Anal. Chem.* **2013**, *6*, 329.
(18) Güell, A. G.; Ebejer, N.; Snowden, M. E.; Macpherson, J. V.; Unwin, P. R. *J. Am. Chem. Soc.* **2012**, *134*, 7258.
(19) Lai, S. C. S.; Dudin, P. V.; Macpherson, J. V.; Unwin, P. R. *J. Am. Chem. Soc.* **2011**, *133*, 10744.
(20) Güell, A. G.; Meadows, K. E.; Dudin, P. V.; Ebejer, N.; Macpherson, J. V.; Unwin, P. R. *Nano Lett.* **2014**, *14*, 220.
(21) Wiggins-Camacho, J. D.; Stevenson, K. J. *J. Phys. Chem. C* **2011**, *115*, 20002.
(22) Fan, Y.; Goldsmith, B. R.; Collins, P. G. *Nat. Mater.* **2005**, *4*, 906.
(23) Dudin, P. V.; Snowden, M. E.; Macpherson, J. V.; Unwin, P. R. *ACS Nano* **2011**, *5*, 10017.
(24) Güell, A. G.; Ebejer, N.; Snowden, M. E.; McKelvey, K.; Macpherson, J. V.; Unwin, P. R. *Proc. Natl. Acad. Sci. U.S.A.* **2012**, *109*, 11487.
(25) Cheng, Y.; Zhang, H.; Varanasi, C. V.; Liu, J. *Sci. Rep.* **2013**, *3*, No. 3195.
(26) Wei, D.; Liu, Y.; Cao, L.; Zhang, H.; Huang, L.; Yu, G.; Kajiura, H.; Li, Y. *Adv. Funct. Mater.* **2009**, *19*, 3618.
(27) Jirkovsky, J. S.; Halasa, M.; Schiffrin, D. J. *Phys. Chem. Chem. Phys.* **2010**, *12*, 8042.
(28) Jirkovský, J. S.; Panas, I.; Ahlberg, E.; Halasa, M.; Romani, S.; Schiffrin, D. J. *J. Am. Chem. Soc.* **2011**, *133*, 19432.
(29) Edwards, J. K.; Solsona, B.; N, E. N.; Carley, A. F.; Herzing, A. A.; Kiely, C. J.; Hutchings, G. J. *Science* **2009**, *323*, 1037.